Active chiral control of GHz acoustic whispering-gallery modes

Sylvain Mezil, Kentaro Fujita, Paul H. Otsuka, Motonobu Tomoda, Matt Clark, Oliver B. Wright, and Osamu Matsuda

Citation: Appl. Phys. Lett. **111**, 144103 (2017); doi: 10.1063/1.4994886

View online: http://dx.doi.org/10.1063/1.4994886

View Table of Contents: http://aip.scitation.org/toc/apl/111/14

Published by the American Institute of Physics

Active chiral control of GHz acoustic whispering-gallery modes

Sylvain Mezil,[1] Kentaro Fujita,[1] Paul H. Otsuka,[1] Motonobu Tomoda,[1] Matt Clark,[2] Oliver B. Wright,[1] and Osamu Matsuda[1,a)]

[1]*Division of Applied Physics, Graduate School of Engineering, Hokkaido University, Sapporo 060-8628, Japan*

[2]*Division of Electrical Systems and Optics, University of Nottingham, Nottingham, NG7 2RD, United Kingdom*

(Received 8 July 2017; accepted 8 September 2017; published online 3 October 2017)

We selectively generate chiral surface-acoustic whispering-gallery modes in the gigahertz range on a microscopic disk by means of an ultrafast time-domain technique incorporating a spatial light modulator. Active chiral control is achieved by making use of an optical pump spatial profile in the form of a semicircular arc, positioned on the sample to break the symmetry of clockwise- and counterclockwise-propagating modes. Spatiotemporal Fourier transforms of the interferometrically monitored two-dimensional acoustic fields measured to micron resolution allow individual chiral modes and their azimuthal mode order, both positive and negative, to be distinguished. In particular, for modes with 15-fold rotational symmetry, we demonstrate ultrafast chiral control of surface acoustic waves in a micro-acoustic system with picosecond temporal resolution. Applications include nondestructive testing and surface acoustic wave devices. *Published by AIP Publishing.* [http://dx.doi.org/10.1063/1.4994886]

Whispering-gallery modes (WGMs) are waves confined to curved interfaces that are guided because of the boundary curvature. First being observed by Lord Rayleigh in the Whispering Gallery of St. Paul's Cathedral in London[1] in the context of acoustics, they have subsequently been observed in many other domains of science,[2] including optics, on geometries such as spheres, cylinders, or disks. Maximum information about such modes can be derived by spatial imaging of the mode field. This was first achieved in optics in a cylindrical silicon-nitride microcavity by use of visible light[3] and later in acoustics in a microscopic copper disk using ∼1 GHz surface acoustic waves (SAWs).[4,5]

In the case of acoustics, WGM-like modes are used in different applications such as in the non-destructive testing of pipes, and various cylindrical geometries have been investigated numerically or experimentally, including by means of laser acoustics[6–9] and picosecond surface-wave acoustics.[4,5] In spite of these investigations, few studies[2] have been specifically designed to break the symmetry in the rotation direction of acoustic WGMs in spite of this being an interesting and topical subject for optical WGMs,[10,11] and, in particular, none have involved acoustic active control.

In order to excite modes with a given chirality in this way, one needs control over the wave propagation direction. In classical ultrasonics, generating acoustic waves in a specific direction can be done by appropriate transducer design, whereas in laser ultrasonics, one can either use moving beams to match the phase velocity[12] or, alternatively, use beam shaping with appropriate optical elements[13] or spatial light modulators.[14–16]

In this paper, we implement the methods of ultrafast laser acoustics for the active control of the chirality of surface-acoustic WGM-like modes at ∼1 GHz in a microscopic disk by use of a spatial light modulator (SLM) and perform time-resolved two-dimensional surface-wave imaging and Fourier analysis to measure the amplitude ratio between clockwise (CW) and counterclockwise (CCW) WGMs.

The experimental setup is shown in Fig. 1(a). The light of wavelength 830 nm from a mode-locked Ti-Sapphire laser with a repetition frequency of $f_{rep} = 75.69$ MHz and a temporal pulse width of ∼100 fs is divided into two beams. One beam is frequency doubled (to 415 nm) for use as a pump beam with a pulse energy of ∼0.25 nJ. It is chopped by an electro-optic modulator at a frequency of $f_p = 1$ MHz. We implement an arbitrary frequency technique[5,17,18] to access the lower and upper sidebands of the acoustic signal, i.e., at $f_{gen} = nf_{rep} + mf_p$, where $n \geq 0$ is a positive integer or zero, and $m = \pm 1$ correspond to the lower sideband (LSB, $m = -1$) or upper sideband (USB, $m = 1$). The pump beam is reflected by a SLM at an angle close to normal incidence to illuminate

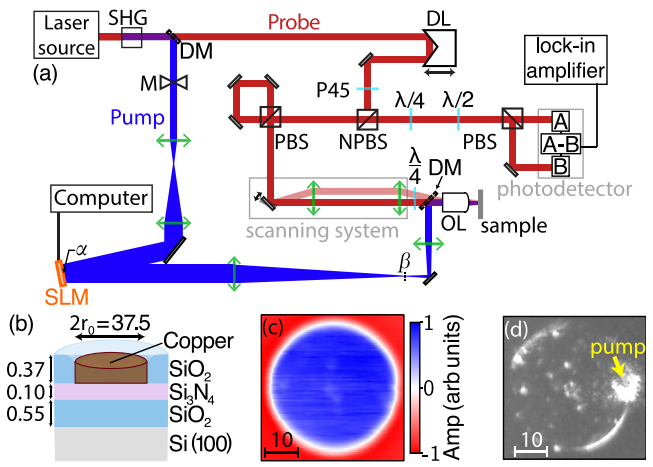

FIG. 1. (a) Diagram of the experimental setup. SHG, second harmonic generator; DM, dichroic mirror; DL, delay line; M, modulator; SLM, spatial light modulator; (N) PBS, (Non-) polarized beam splitter; P45, polarizer oriented at 45° to the vertical; and OL, objective lens. (b) Schematic representation of the sample. (c) Normalized probe reflectivity map. (d) Optical image of the disk and the pump source corresponding to the lower arc. (b)–(d) Dimensions in microns.

a)Electronic mail: omatsuda@eng.hokudai.ac.jp

all SLM phase-retardation-controlled reflectors simultaneously. An appropriate phase retardation pattern, determined by a computer generated hologram (CGH), allows the arbitrary tailoring of the reflected pump beam shape.[19] The CGH is calculated for the far field, corresponding to a Fourier plane in the plane of the SLM [see the point marked by α in Fig. 1(a)], and the reflected pump beam is converted into a real image by a lens [point β in Fig. 1(a)]. This image is relayed by another lens and a microscope objective to the sample surface at normal incidence for thermoelastic acoustic-wave generation, with typical displacements up to $\sim$10 pm.

A second beam of wavelength 830 nm is used as a probe beam, with a pulse energy of $\sim$0.03 nJ, and is focused on the sample surface with the microscope objective, which is also used for the pump beam as described above, to a spot diameter of $\sim 1\,\mu$m. A delay line [DL in Fig. 1(a)] controls the delay time between the pump and probe pulse arrival at the sample. A motorized two-axis tilted mirror associated with relay optics [the scanning system in Fig. 1(a)] scans the probe-beam spot position on the disk surface, whereas the pump light spot position is fixed. This allows the spatiotemporal imaging of the surface acoustic field. The phase of the reflected probe light modulated by the out-of-plane sample surface motion is monitored with a Sagnac interferometer. Lock-in detection allows resolution of surface displacements $\sim$0.2 pm at a bandwidth of $\sim$1 kHz.

The sample, made by International Sematech, is shown schematically in Fig. 1(b). It has the same geometry as that used in previous experiments[4,5] and consists of a polycrystalline copper disk of radius $r_0 = 18.75\,\mu$m embedded in a silicon oxide layer (thickness, 370 nm) lying on a silicon nitride layer (thickness, 100 nm), another silicon oxide layer (thickness 550 nm), and a Si (100) substrate. Polishing the sample to remove the excess deposited copper results in a concave disk surface;[4,20] atomic-force microscopy measurements indicate that the center of the disk is recessed with respect to the surface of the silicon oxide layer by $\sim$150 nm. In contrast to the case of WGMs on a cylinder or in a cylindrical enclosure, in our sample the WGMs are quasi-confined in two-dimensions near the rim of the copper disk by the silicon oxide walls.

The generated WGM acoustic field displacement, u, associated with the generated acoustic frequencies f_{gen} ($f_{\text{gen}} = nf_{\text{rep}} + mf_p$) can be expressed as

$$u(r,\theta,t) = \sum_{n\ell m} A_{n\ell m}(r)\cos\left[\ell\theta - 2\pi f_{\text{gen}} t + \phi_{n\ell m}(r)\right], \quad (1)$$

where (r, θ) is the spatial position in polar coordinates, t is the elapsed time, and ℓ is an integer specifying the azimuthal order. Positive ℓ corresponds to CCW-propagating waves, whereas negative ℓ corresponds to CW-propagating waves. For the summation, n, ℓ, and m take integer values with $n \geq 0$ and $m = \pm 1$, but without the term $(n,m) = (0,-1)$. The Fourier mode amplitude $A_{n\ell m}$ and the initial phase $\phi_{n\ell m}$ are functions of the radial coordinate r only.

The photo-detector output of the interferometer is fed to the lock-in amplifier, and the in-phase (X) and the quadrature components (Y) of its output (proportional to the outward acoustic surface particle velocity) are recorded as a function of delay time (τ) and probe spot position (r, θ). The complex signal $Z = X + iY$ is related to the quantities in Eq. (1) through[18]

$$Z(r,\theta,\tau) = \sum_{n\ell m} \frac{A_{n\ell m}(r)}{2} e^{im\left[\ell\theta - 2\pi n f_{\text{rep}}\tau + \phi_{n\ell m}(r)\right]}, \quad (2)$$

where the summation range is the same as that in Eq. (1). $Z(r, \theta, \tau)$ is also expressed in the form

$$Z(r,\theta,\tau) = \sum_{\ell n'} F_Z(r,\ell,n') e^{i(\ell\theta - 2\pi n' f_{\text{rep}}\tau)},$$
$$F_Z(r,\ell,n') = \frac{1}{2\pi T}\int_0^{2\pi} d\theta \int_0^{T} d\tau Z(r,\theta,\tau) e^{-i(\ell\theta - 2\pi n' f_{\text{rep}}\tau)}, \quad (3)$$

where ℓ, n' are integers. Note that $n' < 0$ is also included here. Comparing Eqs. (2) and (3), we obtain

$$A_{n\ell m}(r) e^{im\phi_{n\ell m}(r)} = 2F_Z(r, m\ell, mn), \quad (4)$$

which allows one to retrieve the acoustic Fourier mode amplitude and initial acoustic phase from the spatiotemporal acoustic data. The CCW (CW) for the USB ($m > 0$) is obtained through $F_Z(r, \ell > 0, n)$ ($F_Z(r, \ell < 0, n)$), whereas the CCW (CW) for the LSB ($m < 0$) is obtained through $F_Z(r, -\ell < 0, -n)$ ($F_Z(r, -\ell > 0, -n)$).

It is possible with this analysis to distinguish WGMs from other acoustic modes in the disk: the former (for $|\ell| > 0$ and relatively low radial mode order) are mainly concentrated in an annulus of width of $\sim\Lambda$ near the disk rim, where $\Lambda \sim 2\pi r/\ell$ is the (WGM) acoustic wavelength (r being the radius of the maximum in A_{nlm}).

To control the propagation direction of the WGMs, we break the symmetry associated with the sign of the angle θ by means of the pump spot shape. An optical source which can be varied under SLM control is used to excite the WGM modes. In this paper, three different spatial patterns are used to generate the acoustic waves: an upper semicircular arc (denoted "$\cap$"), a lower semicircular arc (denoted "$\cup$"), and a point source (denoted "$\circ$") [see Figs. 2(a)–2(c)]. The center of these sources are positioned near the right edge of the disk (at $\sim 2\,\mu$m from the rim in the three cases), where the WGM acoustic energy is localized.

For the point source [$\sim 3.5\,\mu$m at FWHM (full-width at half maximum) diameter], no chirality is expected in the WGM generation, and the CW/CCW Fourier amplitude ratio R° is expected to be unity. For the semicircular arc sources ($\sim 6\,\mu$m in mean diameter and $\sim 2.5\,\mu$m in FWHM thickness), the situation differs. We shall see that the SAW focused to the arc center is observed in the experiment to provide more acoustic energy for WGM generation than the diverging wave propagating oppositely. Therefore, the lower arc favours CCW WGMs, whereas the upper one favours CW WGMs. It is difficult in general to predict the exact ratio of CW to CCW WGMs provided by such a source of broken symmetry in the sign of θ, but it is clear that the chosen arcs, each equivalent to a superposition of multiple point sources, the combination of which break this symmetry, should in general lead by wave interference to chiral WGM generation.

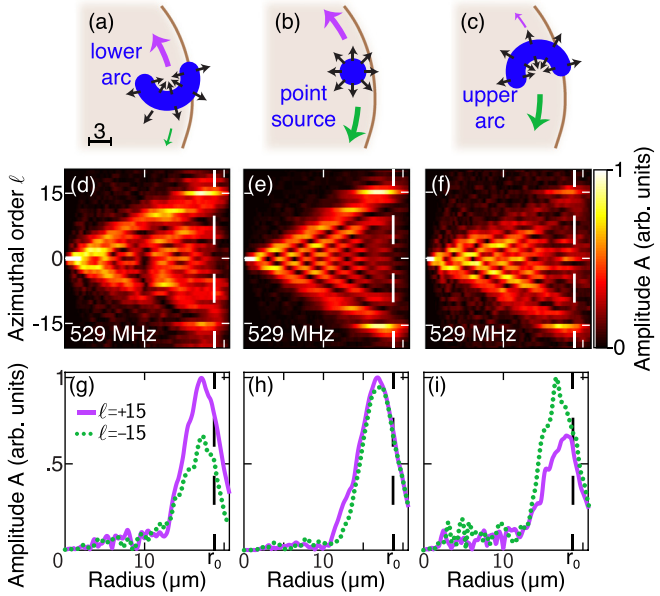

FIG. 2. (a)–(c) Diagram showing the pump source shapes on the disk: (a) lower arc, (b) point source, and (c) upper arc. Dimensions in (a) are in microns. (d)–(i) Plots of the Fourier amplitude $A_{n\ell m}(r)$ at the frequency of $f = 529$ MHz (d)–(f) as a function of the azimuthal order ℓ and the radius r and (g)–(i) as a function of the radius r for $\ell = \pm 15$. Subfigures (d) and (g), (e), and (h), and (f) and (i) correspond to cases (a)–(c), respectively. All plots are independently normalized.

The experimental results for our choice of $f_p = 1$ MHz allow us to access the following azimuthal orders for the lowest order radial mode: $\ell = 9$, 12, 15, 22, 26, and 31, in accordance with the WGM frequency vs ℓ dispersion relation for an identical sample.[5] However, the higher order azimuthal modes $\ell > 15$ have higher spatial frequencies (shorter wavelengths) than we can expect to generate with our optical sources of finite focused line widths. For $\ell = 15$, the WGM acoustic wavelength Λ of $\sim 8\,\mu$m corresponds to ~ 2 times the point source diameter, and for this reason, $\ell = 15$ provides the best match among the excited ℓ values. The experimental results derived from our spatiotemporal dataset for the Fourier amplitude $A_{n\ell m}(r)$ as a function of the azimuthal order ℓ and radius r at a frequency of $f = 529$ MHz ($n = 7$, $m = -1$) are shown in Figs. 2(d)–2(f). The areas inside the triangular region in Figs. 2(d)–2(f) correspond to freely propagating SAWs rather than to the guided WGMs.[4] The latter lie on the upper and lower edges of this triangle. For the point source, the symmetry between $\ell > 0$ and $\ell < 0$ is clear in Fig. 2(e), whereas for the arc sources, different Fourier amplitudes for counter-propagating waves are evident: WGMs with positive (negative) azimuthal order have a larger amplitude when the lower (upper) arc source is used. The mode with the highest Fourier amplitude at this frequency corresponds to $\ell = \pm 15$ and fits well on the previously measured dispersion curves.[5] Cross-sectional views of the amplitude $A_{n\ell m}(r)$ at $\ell = \pm 15$ are plotted in Figs. 2(g)–2(i). The CW/CCW Fourier amplitude ratios are $R_{15}^{\circ} = 1.05$, $R_{15}^{\cap} = 1.51$, and $R_{15}^{\cup} = 0.66$ (the last two being the approximate reciprocal of one another, as expected). The Fourier amplitude radial profiles in Figs. 2(g)–2(i) have been independently normalized; before normalization, the point source amplitude is ~ 3 times larger than in the case of the semicircular arcs. This difference can be attributed to part of the laser energy being focused outside the disk region for the arc sources [see Figs. 1(d), 2(a), and 2(c)] and the presence of destructive wave interference for this case. The estimate of the SAW velocities at 529 MHz is ~ 3800 m/s for the WGMs, assuming an r value equal to the radius of the maximum in A_{nlm} [at $r = 17.1\,\mu$m, see Figs. 2(g)–2(i)] and ~ 3600 m/s for the surface waves travelling across the disk. These velocities lie between the Rayleigh wave velocities in silica and silicon, as expected.[21,22]

Our results can also be presented in two spatial dimensions. From Eqs. (1) and (4), the surface particle velocity as a function of space and time can be expressed for a mode of azimuthal order ℓ at frequency f_{gen} in the form

$$A_{n\ell m}(r)\cos\left[\ell\theta - 2\pi f_{\text{gen}}t + \phi_{n\ell m}(r)\right] = \text{Re}\{2F_Z(r, m\ell, mn)\exp\left[im(\ell\theta - 2\pi f_{\text{gen}}t)\right]\}. \quad (5)$$

This allows the direct spatiotemporal visualization of the surface particle velocity of individual modes in the disk. The images in Figs. 3(a)–3(c) correspond to the sum of the surface particle velocities for the $\ell = -15$ and $\ell = +15$ modes at 529 MHz at a given time for the three measured cases: lower arc, point source, and upper arc, respectively. Associated animations, which are constructed by incrementing the phase in intervals that are small compared with the period, show clearly the dominance of CCW and CW senses of rotation for the cases of Figs. 3(a) and 3(c), respectively (Multimedia view).

WGMs for $\ell = 9$, 12, and 22 are also observed at frequencies in agreement with the frequency vs ℓ dispersion curve.[5] In all these cases, we find that the lower (upper) arc enhances CCW (CW) waves compared to the reference (point source) case, as observed for $\ell = 15$, although accurate values for the ratios R could not be obtained for these other ℓ values. Further measurements are required to identify trends that would allow one to pinpoint why a particular value of ℓ should have better chiral contrast than others, for example.

In conclusion, we have used the techniques of time-domain ultrafast laser acoustics to actively control the chirality of surface-acoustic WGMs. This was achieved by means of a spatial-light modulator to focus the optical pump spot to an appropriately oriented semicircular arc, and we demonstrated significant contrast in the Fourier amplitude ratio between GHz CW and CCW modes. This approach opens the way to control the chirality of surface-acoustic modes in

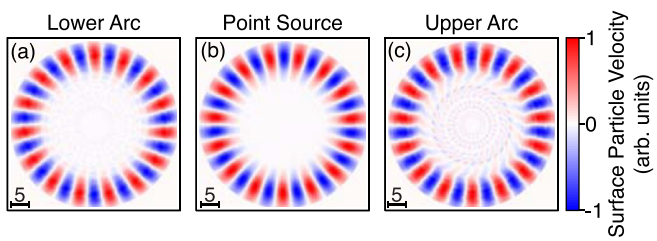

FIG. 3. Plots of the sum of the surface particle velocities for $|\ell| = 15$ at 529 MHz at a given time for (a) the lower arc, (b) the point source, and (c) the upper arc. All plots are independently normalized. Dimensions are in microns. Animations are also viewable. (Multimedia view) [URL: http://dx.doi.org/10.1063/1.4994886.1]

more complicated WGM structures. In future, investigation of the acoustic field generated with different asymmetric source shapes, including different radial distributions, would allow the optimization of the chirality of the generation for a given mode, i.e., the optimization of the CW/CCW amplitude ratio. The theoretical calculation of the acoustic field distribution and power flow for any source shape, as well as simulations of such experiments, would help in the understanding the origin of the chirality and its dependence on the source shape. It should be possible, for example, to find source shapes that achieve near 100% chiral control. To this end, the use of spatiotemporal control rather than just spatial control of the pump light would allow more degrees of freedom. Promising applications of this approach include the characterization of SAW devices and non-destructive testing.

S. Mezil is an International Research Fellow of the Japanese Society for the Promotion of Science (JSPS). This work was partially supported by a Grant-in-Aid for Scientific Research from the Japan Society for the Promotion of Science (17H02807, 16K13713, and 16H03997), by a Research Grant from the Murata Science Foundation. Matt Clark is supported by the EPSRC Grant No. EP/K021877/1.

[1]L. Rayleigh, Philos. Mag. **20**, 1001 (1910).
[2]O. Wright, Phys. World **25**, 31 (2012).
[3]M. L. M. Balistreri, D. W. Klunder, F. C. Blom, A. Driessen, H. W. J. M. Hoekstra, J. P. Korterik, L. Kuipers, and N. F. van Hulst, Opt. Lett. **24**, 1829 (1999).
[4]T. Tachizaki, O. Matsuda, A. A. Maznev, and O. B. Wright, Phys. Rev. B **81**, 165434 (2010).
[5]S. Mezil, P. H. Otsuka, S. Kaneko, O. B. Wright, M. Tomoda, and O. Matsuda, Opt. Lett. **40**, 2157 (2015).
[6]W. Hassan and P. B. Nagy, J. Acoust. Soc. Am. **101**, 2496 (1997).
[7]D. Clorennec and D. Royer, Appl. Phys. Lett. **82**, 4608 (2003).
[8]Y. Fan, F. Honarvar, A. N. Sinclair, and M.-R. Jafari, J. Acoust. Soc. Am. **113**, 102 (2003).
[9]J. W. Dickey, G. V. Frisk, and H. Überall, J. Acoust. Soc. Am. **59**, 1339 (1976).
[10]J. Wiersig, Phys. Rev. A **84**, 063828 (2011).
[11]F.-J. Shu, C.-L. Zou, X.-B. Zou, and L. Yang, Phys. Rev. A **94**, 013848 (2016).
[12]K. Yamanaka, Y. Nagata, and T. Koda, Appl. Phys. Lett. **58**, 1591 (1991).
[13]J. A. Rogers, A. A. Maznev, M. J. Banet, and K. A. Nelson, Ann. Rev. Mater. Sci. **30**, 117 (2000).
[14]P. Cielo, F. Nadeau, and M. Lamontagne, Ultrasonics **23**, 55 (1985).
[15]Y. Hong, S. D. Sharples, M. Clark, and M. G. Somekh, Ultrasonics **42**, 515 (2004).
[16]S. D. Sharples, M. Clark, and M. G. Somekh, Opt. Express **14**, 10435 (2006).
[17]S. Kaneko, O. Matsuda, and M. Tomoda, AIP Adv. **4**, 017124 (2014).
[18]O. Matsuda, S. Kaneko, O. B. Wright, and M. Tomoda, IEEE Trans. Ultrason. Ferroelectr. Freq. Control **62**, 584 (2015).
[19]M. Clark, S. D. Sharples, and M. G. Somekh, J. Acoust. Soc. Am. **107**, 3179 (2000).
[20]A. A. Maznev, T. A. Kelf, M. Tomoda, O. Matsuda, and O. B. Wright, J. Appl. Phys. **107**, 033521 (2010).
[21]R. E. Vines, M. R. Hauser, and J. P. Wolfe, Z. Phys. B **98**, 255 (1995).
[22]*CRC Handbook of Chemistry and Physics*, edited by W. M. Haynes, 91st ed. (CRC Press, 2010).